



Sparse Functional Boxplots for Multivariate Curves

Zhuo Qu  and Marc G. Genton 

Statistics Program, King Abdullah University of Science and Technology, Thuwal, Saudi Arabia

ABSTRACT

This article introduces the sparse functional boxplot and the intensity sparse functional boxplot as practical exploratory tools. Besides being available for complete functional data, they can be used in sparse univariate and multivariate functional data. The sparse functional boxplot, based on the functional boxplot, displays sparseness proportions within the 50% central region. The intensity sparse functional boxplot indicates the relative intensity of fitted sparse point patterns in the central region. The two-stage functional boxplot, which derives from the functional boxplot to detect outliers, is furthermore extended to its sparse form. We also contribute to sparse data fitting improvement and sparse multivariate functional data depth. In a simulation study, we evaluate the goodness of data fitting, several depth proposals for sparse multivariate functional data, and compare the results of outlier detection between the sparse functional boxplot and its two-stage version. The practical applications of the sparse functional boxplot and intensity sparse functional boxplot are illustrated with two public health datasets. Supplementary materials and codes are available for readers to apply our visualization tools and replicate the analysis.

ARTICLE HISTORY

Received March 2021

Accepted April 2022

KEYWORDS

Depth; Missing values;
Multivariate functional data;
Outlier detection; Sparse
functional data; Visualization

1. Introduction

Functional data analysis (Ramsay and Dalzell 1991) regards each observation unit as a function of an index displayed as a curve or image. Descriptive statistics, such as median (Sun and Genton 2012b, Qu, Dai, and Genton 2021) and outliers (Dai and Genton 2019), need to be determined before the functional data can be displayed for exploratory data analysis. Ordering the samples of curves and images directly is difficult. Therefore, many functional depths have been proposed that establish the center of the functional data sample and then order them from the center outwards. Available functional depths in a marginal perspective are the integrated depth (Ibrahim and Molenberghs 2009), random projection depth (Cuevas, Febrero, and Fraiman 2007), random Tukey depth (Cuesta-Albertos and Nieto-Reyes 2008), band and modified band depth (López-Pintado and Romo 2009), half-region depth and modified half-region depth (López-Pintado and Romo 2011), functional spatial depth (Sguera, Galeano, and Lillo 2014), and extremal depth (Narisetty and Nair 2016). Moreover, multivariate functional depths have been proposed based on two generalizations: from functional to multivariate functional scenarios and from multivariate to multivariate functional scenarios. Examples of the first idea include the weighted average of the marginal functional depths (Ieva and Paganoni 2013) and the simplicial and modified simplicial band depths (López-Pintado et al. 2014). An example of the second idea is the multivariate functional halfspace depth (Claeskens et al. 2014).

With the intensive development of different depth notions, various tools have been developed for visualizing functional

data and detecting outliers. Hyndman and Shang (2010) made use of the first two robust functional principal component scores and presented functional versions of the bagplot and the highest density region plot. With the modified band depth giving the ranks among data, Sun and Genton (2011) proposed the functional boxplot, a potent analog to the classical boxplot (Tukey 1975), for visualizing functional data. For functional data with a dependence structure, Sun and Genton (2012a) provided an adaptive way of determining the outlier selection factor in the adjusted functional boxplot. Arribas-Gil and Romo (2014) explored the relationship between modified band depth and modified epigraph index (López-Pintado and Wei 2011) and proposed the outliergram to visualize and detect shape outliers among functional data. Genton et al. (2014) introduced a surface boxplot based on the modified volume depth and developed an interactive surface boxplot tool for the visualization of samples of images. Mirzargar, Whitaker, and Kirby (2014) extended the notion of depths from functional data to curves, presenting the curve boxplot for visualizing ensembles of 2D and 3D curves. Dai and Genton (2018a) developed a two-stage functional boxplot for multivariate curves, combining directional outlyingness (Dai and Genton 2019) and a classical functional boxplot in the outlier detection procedure. Additionally, Dai and Genton (2018b) introduced the magnitude-shape (MS) plot for visualizing both the magnitude and shape outlyingness of multivariate functional data. Yao, Dai, and Genton (2020) proposed the trajectory functional boxplot and the modified simplicial band depth (MSBD) versus wiggliness of directional outlyingness (WO) plot for visualizing trajectory

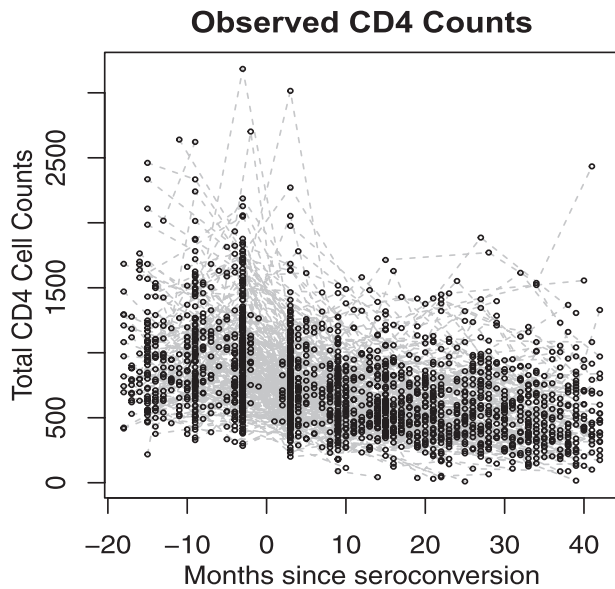


Figure 1. Observed CD4 cell counts from 366 patients (black solid points) measured from 18 months before to 42 months after seroconversion (the time period during which a specific antibody develops and becomes detectable in the blood).

functional data. For more visualization examples, see the recent review of Genton and Sun (2020).

The above visualization techniques can only be applied to samples of curves measured on fine and common grids. In practice, the grids are not always fine or common; rather, curves are sometimes observed on sparse or irregularly spaced time points. Figure 1 shows a longitudinal study of CD4 cell counts (Goldsmith, Greven, and Crainiceanu 2013) per milliliter of blood to track the progress of HIV. Overall, there are 366 patients, with between 1 and 11 observations per subject and a mean of 5, yielding 1888 data points. Figure 2 presents a dataset of malnutrition metrics, consisting of the prevalence of stunted growth and low birth weight, between 1985 and 2019 for 77 countries. Sparseness appears randomly for the first variable, stunted growth, and values for low birth weight are only available for years 2000 to 2015. Applying visualization tools to sparse functional data is difficult but necessary in order to visualize sparse multivariate functional data.

Various ideas have been proposed to deal with missingness in the notion of depth in the univariate functional case. A first approach is to fit the sparse functional data before applying current univariate depths and a second approach is to revise the notions of depth for the sparse functional data case. One example of the first approach is in López-Pintado and Wei (2011), in which the ideas of univariate functional principal component analysis (UFPCA, Yao, Müller, and Wang 2005) are applied for sparse data fitting and the modified band depth is used to order the fitted data. Other available methods for fitting sparse functional data include UFPCA under different frameworks (James, Hastie, and Sugar 2000, Liu, Ray, and Hooker 2017), B-spline models (Thompson and Rosen 2008), and covariance estimation (Xiao et al. 2018). It is worth noting that Goldsmith, Greven, and Crainiceanu (2013) proposed a bootstrap procedure to improve curve estimates by accounting for both uncertainty in UFPCA decompositions and model-based estimates

based on UFPCA estimates in Yao, Müller, and Wang (2005). Additionally, pointwise and simultaneous confidence bands that account for both model- and decomposition-based variability were constructed. One example of the second approach is in Sguera and López-Pintado (2021), where the idea of depth is extended by incorporating both the curve estimation and its confidence bands (Goldsmith, Greven, and Crainiceanu 2013) into the depth analysis, which can be applied to any univariate functional depth.

Similar methods have been generalized to fit sparse data in the multivariate functional setting. Zhou, Huang, and Carroll (2008) modeled paired longitudinal data with principal components and fitted them by penalized splines under the mixed-effects model framework. However, their method is limited to only two variables when the data are either observed or missing simultaneously. Happ and Greven (2018) proposed a multivariate functional principal component analysis (MFPCA) defined on different time grids, which is also suitable for data with missing values. Li, Xiao, and Luo (2020) derived a fast algorithm for fitting sparse multivariate functional data via estimating the multivariate covariance function with tensor product B-spline. However, a bootstrap procedure was not considered in the sparse multivariate functional data to improve curve estimates. Still, the depth of sparse multivariate functional data has not been considered in detail.

The novel contributions in this article are 3-fold. First, we implement a bootstrap procedure to improve the MFPCA fit (Happ and Greven 2018). Second, we propose a revised depth in the sparse multivariate functional case to determine the order of sparse multivariate functional data. Third, we develop visualization tools for both marginal and joint sparse functional data. The sparse functional boxplot mainly displays the percentage of sparse points within the central region, whereas the intensity sparse functional boxplot highlights the intensity of the sparse points in the central region.

The remainder of the article is organized as follows. The procedure of fitting sparse multivariate functional data and computing depths for sparse multivariate functional data are considered in Section 2. Sparse and intensity sparse functional boxplots, together with their two-stage forms, are presented in Section 3. The depth selection and outlier detection performance for different visualization tools are demonstrated in Section 4. Applications to the aforementioned CD4 and malnutrition data are presented in Section 5. The article ends with a discussion in Section 6.

2. Ordering Sparse Multivariate Functional Data

We consider a two-step procedure to order sparse multivariate functional data: first we generalize the bootstrap procedure (Goldsmith, Greven, and Crainiceanu 2013) from UFPCA to MFPCA (Happ and Greven 2018) to generate improved curve estimates and confidence bands; second, we consider various notions of depth for sparse multivariate functional data. The depth notions we consider are either from the direct generalization of the univariate revised functional depth (Sguera and López-Pintado 2021) to multivariate functional data, or our new idea described in Section 2.2.

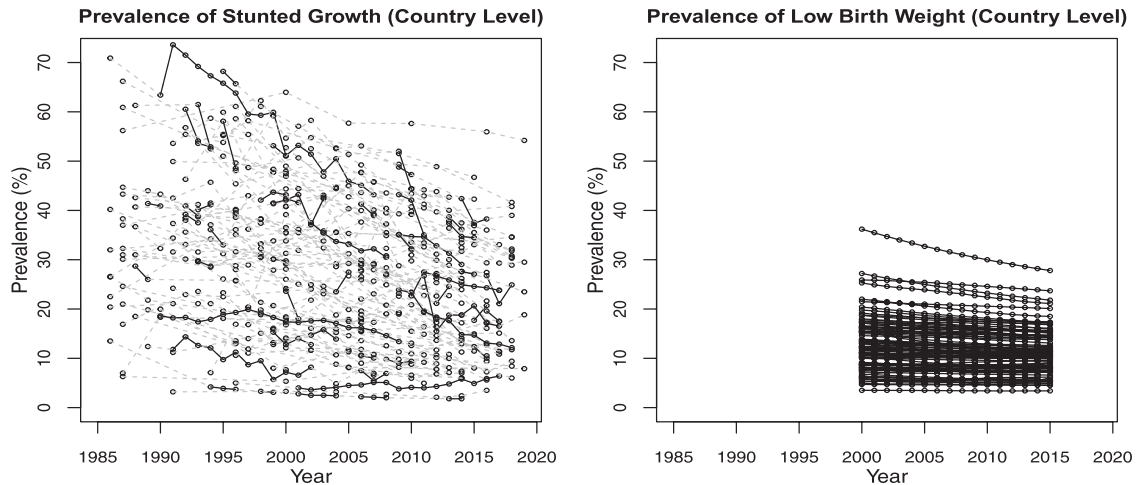


Figure 2. The observed prevalence of stunted growth and prevalence of low birth weight for 77 countries from 1985 to 2019. Observations are joined with solid black lines if observed continuously; otherwise, joined with gray dashed lines.

2.1. Fitting Sparse Multivariate Functional Data

2.1.1. Data Structure and Notation

This article considers multivariate functional data. A multivariate functional random variable \mathbf{Y} (Hsing and Eubank 2015) is a random vector with values in an infinite-dimensional space. A well-received model of multivariate functional data is to consider paths of a stochastic process taking values in some Hilbert space, \mathcal{H} , of functions defined on some set \mathcal{T} . First we consider a p -variate ($p \in \mathbb{Z}_+$) stochastic process $\mathbf{Y}(\mathbf{t}) = (Y^{(1)}(t^{(1)}), \dots, Y^{(p)}(t^{(p)}))^\top$ with $\mathbf{t}^\top := (t^{(1)}, \dots, t^{(p)}) \in \mathcal{T} := \mathcal{T}_1 \times \dots \times \mathcal{T}_p$. Note that \mathbf{t} is a p -dimensional vector, with its element $t^{(j)}$ being a random time and independent of all other random variables. Each element $Y^{(j)}(t^{(j)})$ ($j = 1, \dots, p$) is defined on the domain \mathcal{T}_j , where the \mathcal{T}_j s are compact sets in \mathbb{R} with finite Lebesgue measure. Briefly speaking, $Y^{(j)}(t^{(j)}): \mathcal{T}_j \rightarrow \mathbb{R}$ is assumed to be square-integrable in \mathcal{T}_j , expressed as $L^2(\mathcal{T}_j)$. Second, we consider the p -dimensional functional data $\mathbf{Y} = \{\mathbf{Y}(\mathbf{t})\}_{\mathbf{t} \in \mathcal{T}}$ and we have $\mathbf{Y} \in \mathcal{H}$, where the space $\mathcal{H} := L^2(\mathcal{T}_1) \times \dots \times L^2(\mathcal{T}_p)$.

For $\mathbf{s}, \mathbf{t} \in \mathcal{T}$, define the matrix of covariances $\mathbf{C}(\mathbf{s}, \mathbf{t}) := \text{cov}\{\mathbf{Y}(\mathbf{s}), \mathbf{Y}(\mathbf{t})\}$ with elements $C_{ij}(s^{(i)}, t^{(j)}) := \text{cov}\{Y^{(i)}(s^{(i)}), Y^{(j)}(t^{(j)})\}$ for $s^{(i)} \in \mathcal{T}_i$ and $t^{(j)} \in \mathcal{T}_j$. Define the covariance operator $\Gamma : \mathcal{H} \rightarrow \mathcal{H}$ with the j th element of Γf for $f \in \mathcal{H}$ given by $(\Gamma f)^{(j)}(t^{(j)}) := \sum_{i=1}^p \int_{\mathcal{T}_i} C_{ij}(s^{(i)}, t^{(j)}) f^{(i)}(s^{(i)}) ds^{(i)}$ for $t_j \in \mathcal{T}_j$. By the Hilbert-Schmidt Theorem (Renardy and Rogers 2006, pp. 253–262), it follows that there exists a complete orthonormal basis of eigenfunctions $\boldsymbol{\psi}_m = (\psi_m^{(1)}, \dots, \psi_m^{(p)})^\top \in \mathcal{H}$, $m \in \mathbb{N}$ of Γ such that $\Gamma \boldsymbol{\psi}_m = \nu_m \boldsymbol{\psi}_m$ and $\lim_{m \rightarrow +\infty} \nu_m = 0$.

Here, ν_m is a sequence of nonzero real eigenvalues such that $\nu_1 \geq \nu_2 \geq \dots \geq 0$. In Proposition 2 of Happ and Greven (2018), the covariance operator Γ is a linear, self-adjoint and positive operator. Let $\sum_{m=1}^{\infty} \nu_m \psi_m^{(j)}(s^{(j)}) \psi_m^{(j)}(t^{(j)})$ be the spectral decomposition of $C_{jj}(s^{(j)}, t^{(j)})$. Based on the property of Γ and the decomposition of covariance elements, a multivariate Karhunen-Loève representation (Happ and Greven 2018) for $\mathbf{Y}(\mathbf{t})$ is $\mathbf{Y}(\mathbf{t}) = \boldsymbol{\mu}(\mathbf{t}) + \sum_{m=1}^{\infty} \rho_m \boldsymbol{\psi}_m(\mathbf{t})$ for $\mathbf{t} \in \mathcal{T}$, $\boldsymbol{\mu}(\mathbf{t}) := \mathbb{E}\{\mathbf{Y}(\mathbf{t})\}$ is the mean function $\boldsymbol{\mu}$ evaluated at time \mathbf{t} , with the element $\mu^{(j)}(t^{(j)}) = \mathbb{E}\{Y^{(j)}(t^{(j)})\}$ for $j = 1, \dots, p$, and $\boldsymbol{\psi}_m(\mathbf{t})$

is the m th ($m \in \mathbb{N}$) eigenfunction evaluated at time \mathbf{t} . Here, $\rho_m = \sum_{j=1}^p \int_{\mathcal{T}_j} \{Y^{(j)}(t^{(j)}) - \mu^{(j)}(t^{(j)})\} \psi_m^{(j)}(t^{(j)}) dt^{(j)}$ are zero mean random variables with $\text{cov}(\rho_m, \rho_n) = \nu_m$ if $m = n$, and $\text{cov}(\rho_m, \rho_n) = 0$ if $m \neq n$ for $m, n \in \mathbb{N}$.

In the following, let $\mathbf{Y}_1, \dots, \mathbf{Y}_N$ be a set of independent observations of \mathbf{Y} . In practice, we observe the functions $\mathbf{Y}_i(\mathbf{t})$ ($i = 1, \dots, N$) with error $\boldsymbol{\epsilon}_i(\mathbf{t}) = (\epsilon_i^{(1)}(t^{(1)}), \dots, \epsilon_i^{(p)}(t^{(p)}))^\top$, and the element $\epsilon_i^{(j)}(t^{(j)}) \stackrel{\text{iid}}{\sim} \mathcal{N}(0, \sigma_j^2)$. Moreover, the functions $\mathbf{Y}_i(\mathbf{t}_i)$ are observed on sparse finite grids at the subject and element level, that is, the j th ($j = 1, \dots, p$) element $t_i^{(j)}$ of \mathbf{t}_i ($\mathbf{t}_i \in \mathcal{T}$) can vary per curve. Let the observed functions with measurement errors and the sparseness be $\tilde{\mathbf{Y}}_i(\mathbf{t}_i)$ such that $\tilde{\mathbf{Y}}_i(\mathbf{t}_i) = \mathbf{Y}_i(\mathbf{t}_i) + \boldsymbol{\epsilon}_i(\mathbf{t}_i)$.

Then, the estimation of observed functions $\tilde{\mathbf{Y}}_i(\mathbf{t}_i)$ can be approximated by the multivariate truncated Karhunen-Loève expansions (Happ and Greven 2018) $\bar{\mathbf{Y}}_i(\mathbf{t}_i)$ such that $\bar{\mathbf{Y}}_i(\mathbf{t}_i) = \boldsymbol{\mu}(\mathbf{t}_i) + \sum_{m=1}^M \rho_{i,m} \boldsymbol{\psi}_m(\mathbf{t}_i) + \boldsymbol{\epsilon}_i(\mathbf{t}_i)$. Here, M is the minimal number of eigenfunctions that explain 99% variability in the observed curves. Define $\boldsymbol{\Psi} = (\boldsymbol{\psi}_1, \dots, \boldsymbol{\psi}_M)$ the collection of the first M eigenfunctions, $\mathbf{V} = \text{diag}\{\nu_1, \dots, \nu_M\}$, $\boldsymbol{\Sigma} = \text{diag}\{\sigma_1^2, \dots, \sigma_p^2\}$. We name the decomposition objects $\boldsymbol{\theta} = \{M, \boldsymbol{\mu}, \boldsymbol{\Psi}, \mathbf{V}, \boldsymbol{\Sigma}\}$. Let the eigenscores for function \mathbf{Y}_i be $\boldsymbol{\rho}_i = \{\rho_{i,m} : m = 1, \dots, M\}$, the estimation of $\boldsymbol{\rho}_i$ is regarded as an expectation based on the objects estimated in the MFPCA decomposition, $\hat{\boldsymbol{\theta}}$. Then, the estimation of $\bar{\mathbf{Y}}_i(\mathbf{t}_i)$ is seen as the expectation of $\tilde{\mathbf{Y}}_i(\mathbf{t}_i)$ based on the estimated $\hat{\boldsymbol{\theta}}$ and $\hat{\boldsymbol{\rho}}_i$. Take a random $\mathbf{t} = (t^{(1)}, \dots, t^{(p)})^\top \in \mathcal{T}$. The estimated j th component of the i th observation at $t^{(j)}$ is expressed as below:

$$\begin{aligned} \hat{Y}_{\hat{\boldsymbol{\theta}}, i}^{(j)}(t^{(j)}) &= \mathbb{E}\left\{\tilde{Y}_i^{(j)}(t^{(j)}) | \hat{\boldsymbol{\rho}}_{\hat{\boldsymbol{\theta}}, i}, \hat{\boldsymbol{\theta}}\right\} \\ &= \hat{\mu}^{(j)}(t^{(j)}) + \sum_{m=1}^M \hat{\rho}_{i,m} \hat{\psi}_m^{(j)}(t^{(j)}), \\ i &= 1, \dots, N, j = 1, \dots, p, t^{(j)} \in \mathcal{T}^{(j)}. \end{aligned} \quad (1)$$

The MFPCA estimation is available in *MFPCA* package (Happ 2018) in R (Ihaka and Gentleman 1996).

2.1.2. Bootstrap Improved Estimation and Confidence Bands

The MFPCA fit is a model-based estimate without taking into account the uncertainty in the decomposition objects. Hence, we implement the bootstrap (Goldsmith, Greven, and Crainiceanu 2013) to combine the model-based conditional estimates across the distribution of decompositions.

Assume we implement the bootstrap with $B = 100$ replicates. We randomly select N functions from observations Y_1, \dots, Y_N with replacement, and obtain the model-based estimate in (1). The bootstrap MFPCA (BMFPCA) fit is obtained from the iterated expectation and we provide the estimated j th component of the i th observation at $t^{(j)}$ as below:

$$\widehat{Y}_i^{(j)}(t^{(j)}) = \mathbb{E}_{\widehat{\theta}} \left[\mathbb{E}_{\widetilde{Y}_i^{(j)}|\widehat{\theta}} \left\{ \widetilde{Y}_i^{(j)}(t^{(j)}) | \widehat{\rho}_{i,i}, \widehat{\theta} \right\} \right], \\ i = 1, \dots, N, j = 1, \dots, p, t^{(j)} \in \mathcal{T}^{(j)}. \quad (2)$$

Like Happ and Greven (2018), we do not assume any distribution for $\rho_{i,m}$. Thus, we use the naive bootstrap to obtain the confidence bands. Given the confidence level α , for each fixed time grid and the component of the curve, we take the $(1 - \frac{\alpha}{2})$ th percentile across the bootstrap as the confidence upper bound, and the $\frac{\alpha}{2}$ th percentile across the bootstrap as the confidence lower bound. Here, we define the j th component of the i th upper bound at $t^{(j)}$ as $Y_{ub,i}^{(j)}(t^{(j)}) := q_{1-\frac{\alpha}{2}}(\widehat{Y}_{\theta_{1,i}}^{(j)}(t^{(j)}), \dots, \widehat{Y}_{\theta_{B,i}}^{(j)}(t^{(j)}))$, where $q_\beta(A)$ denotes the β th percentile of the set A . Similarly, the j th component of the i th lower bound at $t^{(j)}$ as $Y_{lb,i}^{(j)}(t^{(j)}) := q_{\frac{\alpha}{2}}(\widehat{Y}_{\theta_{1,i}}^{(j)}(t^{(j)}), \dots, \widehat{Y}_{\theta_{B,i}}^{(j)}(t^{(j)}))$. We can easily obtain $\mathbf{Y}_{ub,i}(t) = (Y_{ub,i}^{(1)}(t^{(1)}), \dots, Y_{ub,i}^{(p)}(t^{(p)}))^\top$ and $\mathbf{Y}_{lb,i}(t) = (Y_{lb,i}^{(1)}(t^{(1)}), \dots, Y_{lb,i}^{(p)}(t^{(p)}))^\top$ with each component given, and the confidence bands bounded by $\mathbf{Y}_{ub,i}$ and $\mathbf{Y}_{lb,i}$.

2.2. Notions of Depth for Sparse Multivariate Functional Data

We take multivariate functional halfspace depth (MFHD, Hubert, Rousseeuw, and Segaert 2015) as an example to represent depth revision in sparse settings in later sections; in principle, any reasonable multivariate functional depth can be used. Since multivariate functional depth (MFD) requires common time grids for all variables, without loss of generality, we let $\mathcal{T}_j = \mathcal{T}$ for $j = 1, \dots, p$, where \mathcal{T} is a compact set in \mathbb{R} . Later, the revised depth can be proposed by applying MFHD to the fitted data (see López-Pintado and Wei 2011 in the univariate sparse functional case), or by taking the depths of fitted data and their confidence bands into account. There are several implementations in the latter case, see Section 2.2.2 for details.

2.2.1. Conventional Depth for Multivariate Functional Data

For \mathbf{X} a random vector on \mathbb{R}^p , let $D(\cdot; F_{\mathbf{X}}) : \mathbb{R}^p \rightarrow [0, 1]$ be a statistical depth function (Zuo and Serfling 2000) for the probability distribution of \mathbf{X} with associated cdf $F_{\mathbf{X}}$. Accordingly, the depth region $D_\beta(F_{\mathbf{X}})$ at level $\beta \geq 0$, is defined as $D_\beta(F_{\mathbf{X}}) = \{\mathbf{X} \in \mathbb{R}^p : D(\mathbf{X}; F_{\mathbf{X}}) \geq \beta\}$. We let $C^p(\mathcal{T})$ be continuous paths for the p -variate continuous functions with $t \in \mathcal{T}$. The definition of MFD combines the local depths at each

time point and includes a weight function that may change with time.

Consider such a p -variate stochastic process $\{\mathbf{X}(t), t \in \mathcal{T}\}$ on \mathbb{R}^p with cdf $F_{\mathbf{X}(t)}$ at each time point t that generates continuous paths in $C^p(\mathcal{T})$. Take an arbitrary $\mathbf{Y} \in C^p(\mathcal{T})$. Let w be a weight function that integrates to one on the domain \mathcal{T} . The MFD of \mathbf{Y} is defined as $MFD(\mathbf{Y}; F_{\mathbf{X}}) = \int_{\mathcal{T}} D(\mathbf{Y}(t); F_{\mathbf{X}(t)})w(t)dt$. Here, if the weight is a constant, then $w(t) := w$; if $w(t)$ changes with time t , then $w(t) := \text{vol}\{D_\beta(F_{\mathbf{X}(t)})\}/\int_{\mathcal{T}} \text{vol}\{D_\beta(F_{\mathbf{X}(u)})\}du$ is proportional to the volume of the depth region at time point t . The population halfspace depth (HD, Tukey 1975) at $\mathbf{Y}(t) \in \mathbb{R}^p$ is $HD(\mathbf{Y}(t); F_{\mathbf{X}(t)}) = \inf_{\mathbf{u} \in \mathbb{R}^p, \|\mathbf{u}\|=1} P\{\mathbf{u}^\top \mathbf{X}(t) \geq \mathbf{u}^\top \mathbf{Y}(t)\}$. Thus, the population definition of MFHD is expressed as

$$MFHD(\mathbf{Y}; F_{\mathbf{X}}) = \int_{\mathcal{T}} HD(\mathbf{Y}(t); F_{\mathbf{X}(t)})w(t)dt. \quad (3)$$

In practice, instead of observing curves, one observes curve evaluations at a set of time points $t_1 < \dots < t_L$ in $\mathcal{T} = [t_1, t_L]$, not necessarily equidistant. Consider a sample of multivariate functional observations $\mathbf{X}^f(t_l) = \{\mathbf{X}_1(t_l), \dots, \mathbf{X}_N(t_l); t_l \in \mathcal{T}\}$ with at each time point t cdf $F_{\mathbf{X}^f(t),N}$. The sample multivariate functional depth at $\mathbf{Y} \in C^p(\mathcal{T})$ is defined with $t_0 = t_1$, $t_{L+1} = t_L$ and $W_l = \int_{(t_{l-1}+t_l)/2}^{(t_l+t_{l+1})/2} \widetilde{w}(t)dt$, by $MFD(\mathbf{Y}; \mathbf{X}^f) = \sum_{l=1}^L D(\mathbf{Y}(t_l); F_{\mathbf{X}^f(t_l),N}) W_l$. Similarly, $W_l = \widetilde{w} \cdot (t_{l+1} - t_{l-1})/2$ if $\widetilde{w}(t)$ is a constant, otherwise $W_l = \text{vol}\{D_\beta(F_{\mathbf{X}^f(t_l),N})\}(t_{l+1} - t_{l-1})/[\sum_{l=1}^L \text{vol}\{D_\beta(F_{\mathbf{X}^f(t_l),N})\}(t_{l+1} - t_{l-1})]$. The finite-sample halfspace depth (HD) is: $HD(\mathbf{Y}(t_l); F_{\mathbf{X}^f(t_l),N}) = \frac{1}{N} \min_{\#\{\mathbf{X}_i(t_l), i = 1, \dots, N : \mathbf{u}^\top \mathbf{X}_i(t_l) \geq \mathbf{u}^\top \mathbf{Y}(t_l)\}}$, where $\#$ represents the number of counts. Therefore, the finite sample definition of MFHD is

$$MFHD(\mathbf{Y}; \mathbf{X}^f) = \sum_{l=1}^L HD(\mathbf{Y}(t_l); F_{\mathbf{X}^f(t_l),N}) W_l. \quad (4)$$

2.2.2. Revised Depth for Sparse Multivariate Functional Data

We let $\widehat{\mathbf{Y}}^f = \{\widehat{\mathbf{Y}}_1, \dots, \widehat{\mathbf{Y}}_N\}$ be a set including N samples of fitted multivariate functional data over dense time grids. We also obtain a set of confidence upper bounds $\widehat{\mathbf{Y}}_{ub}^f = \{\widehat{\mathbf{Y}}_{ub,1}, \dots, \widehat{\mathbf{Y}}_{ub,N}\}$ and confidence lower bounds $\widehat{\mathbf{Y}}_{lb}^f = \{\widehat{\mathbf{Y}}_{lb,1}, \dots, \widehat{\mathbf{Y}}_{lb,N}\}$. We list the revised depth notion in the finite-sample version, and the population version can be analogously derived.

Besides applying the current multivariate functional depths to the fitted data, we consider two additional ideas for revising the notion of depth for sparse multivariate functional data. They define the revised depth of \mathbf{Y}_i ($i = 1, \dots, N$) as the weighted average MFHD of the fitted data $\widehat{\mathbf{Y}}_i$, the confidence upper bound $\widehat{\mathbf{Y}}_{ub,i}$, and the confidence lower bound $\widehat{\mathbf{Y}}_{lb,i}$ in $\widehat{\mathbf{Y}}_{upd} := \{\widehat{\mathbf{Y}}^f, \widehat{\mathbf{Y}}_{ub}^f, \widehat{\mathbf{Y}}_{lb}^f\}$ with different weights. Specifically, the first depth assigns 1/3 to the fitted data, and to each of its confidence upper and lower bounds, which is the same as that in Sguera and López-Pintado (2021) in the univariate sparse functional case, while the second depth assigns 1/2 to the fitted data and 1/4 to its confidence upper and lower

bounds, respectively. The weights in the second depth are new. We name the aforementioned revised depths the average-weight revised depth RMFHD_{aw}, and non-average-weight revised depth RMFHD_{naw}:

$$\begin{aligned} & \text{RMFHD}_{\text{type}}(\widehat{\mathbf{Y}}; \widehat{\mathbf{Y}}_{\text{upd}}) \\ &= \begin{cases} \frac{1}{3} \text{MFHD}(\widehat{\mathbf{Y}}; \widehat{\mathbf{Y}}_{\text{upd}}) + \frac{1}{3} \text{MFHD}(\widehat{\mathbf{Y}}_{\text{ub}}; \widehat{\mathbf{Y}}_{\text{upd}}) \\ \quad + \frac{1}{3} \text{MFHD}(\widehat{\mathbf{Y}}_{\text{lb}}; \widehat{\mathbf{Y}}_{\text{upd}}), & \text{if type = aw,} \\ \frac{1}{2} \text{MFHD}(\widehat{\mathbf{Y}}; \widehat{\mathbf{Y}}_{\text{upd}}) + \frac{1}{4} \text{MFHD}(\widehat{\mathbf{Y}}_{\text{ub}}; \widehat{\mathbf{Y}}_{\text{upd}}) \\ \quad + \frac{1}{4} \text{MFHD}(\widehat{\mathbf{Y}}_{\text{lb}}; \widehat{\mathbf{Y}}_{\text{upd}}), & \text{if type = naw.} \end{cases} \end{aligned} \quad (5)$$

We apply the conventional depth MFHD and its revised forms RMFHD to various data settings in simulations in [Section 4.1](#), and we identify the best depth according to the Spearman rank coefficient in [Section 4.2](#).

3. Construction of Sparse Functional Boxplots

The revised depths in [Section 2](#) make the visualization of sparse multivariate functional data possible. The novel visualization tools coined sparse functional boxplot and intensity sparse functional boxplot not only keep the features of the original functional boxplot ([Sun and Genton 2011](#)) but also display sparseness features. We further add a section illustrating the process of obtaining the two-stage ([Dai and Genton 2018a](#)) version of those two visualization tools. Without loss of generality, we use \mathbf{Z}_i ($i = 1, \dots, N$) to express the fitted data $\widehat{\mathbf{Y}}_i$ and the corresponding set $\mathbf{Z}^f := (\mathbf{Z}_1, \dots, \mathbf{Z}_N)$ in [Section 3](#) and the directional outlyingness is applied to only \mathbf{Z}_i but not its confidence bands.

3.1. Sparse Functional Boxplot

The functional boxplot is constructed given the functional depth values for functional observations. Similar to the classical boxplot ([Tukey 1977](#)), it mainly displays five characteristics: the central region, the median, the outliers, the nonoutlying maximal bound, and the nonoutlying minimal bound. The 50% central region is delimited by the envelope of the 50% deepest curves from the sample set \mathbf{Z}^f . In particular, the sample 50% central region $C_{0.5}$ for the j th ($j = 1, \dots, p$) component is $C_{0.5}^{(j)} = \{(t, Z^{(j)}(t)) : \min_{r=1, \dots, \lceil N/2 \rceil} Z_{[r]}^{(j)}(t) \leq Z^{(j)}(t) \leq \max_{r=1, \dots, \lceil N/2 \rceil} Z_{[r]}^{(j)}(t), t \in \widetilde{\mathcal{T}}\}$, where $\lceil N/2 \rceil$ is the smallest integer not less than $N/2$, and $Z_{[r]}^{(j)}(t)$ is the j th component of the r th deepest curve evaluated at t for $t \in \widetilde{\mathcal{T}}$. The upper bound of the central region evaluated at time t is $Z_{ub,0.5}^{(j)}(t) = \max_{r=1, \dots, \lceil N/2 \rceil} Z_{[r]}^{(j)}(t)$, and the lower bound evaluated at t is $Z_{lb,0.5}^{(j)}(t) = \min_{r=1, \dots, \lceil N/2 \rceil} Z_{[r]}^{(j)}(t)$. We also define the range of $C_{0.5}^{(j)}$ at t as the difference between the upper bound and lower bound that $R_{0.5}^{(j)}(t) := \max_{r=1, \dots, \lceil N/2 \rceil} Z_{[r]}^{(j)}(t) - \min_{r=1, \dots, \lceil N/2 \rceil} Z_{[r]}^{(j)}(t)$. The median $Z_{[1]}^{(j)}(t)$ is the curve with the highest depth.

Then, a curve \mathbf{Z}_o is detected as an outlier, if the measurement of the j th component of \mathbf{Z}_o is higher than the summation of 1.5 times the range of $C_{0.5}^{(j)}$ and the upper bound of $C_{0.5}^{(j)}(t)$ (or lower than the difference between the lower bound of $C_{0.5}^{(j)}$ and 1.5 times the range of $C_{0.5}^{(j)}(t)$) at some time t . That is $Z_o^{(j)}(t) > Z_{ub,0.5}^{(j)}(t) + 1.5R_{0.5}^{(j)}(t)$ or $Z_o^{(j)}(t) < Z_{lb,0.5}^{(j)}(t) - 1.5R_{0.5}^{(j)}(t)$. Let S_o be the set of functional outliers. The nonoutlying maximal (minimal) bound is established by connecting the maximal (minimal) points at all time indexes excluding the outliers. That is, $Z_{ub}^{(j)}(t) = \max_{\mathbf{Z} \in \mathbf{Z}^f \setminus S_o} Z^{(j)}(t)$, and $Z_{lb}^{(j)}(t) = \min_{\mathbf{Z} \in \mathbf{Z}^f \setminus S_o} Z^{(j)}(t)$ for $t \in \widetilde{\mathcal{T}}$.

The sparse functional boxplot, apart from displaying the aforementioned features, underlines the sparseness features in the median $Z_{[1]}^{(j)}(t)$, the 50% central region $C_{0.5}^{(j)}$, and the detected outliers S_o . The median is drawn in black for the observed values and gray for the missing ones ([Figure 3](#), second row). At each time point $t \in \widetilde{\mathcal{T}}$ within $C_{0.5}^{(j)}$, we count the number of missing points $n_{ms}^{(j)}(t)$ and that of observed points $n_{obs}^{(j)}(t)$, and obtain the sparseness proportion $p_s^{(j)}(t)$, which is the number of sparse points divided by the total number of points $n_{ms}^{(j)}(t)/\{n_{ms}^{(j)}(t) + n_{obs}^{(j)}(t)\}$. Then, we define the proportion line such that: $l^{(j)}(t, p_s^{(j)}(t)) := Z_{ub,0.5}^{(j)}(t) - p_s^{(j)}(t)R_{0.5}^{(j)}(t)$ for $t \in \widetilde{\mathcal{T}}$. It is derived from subtracting the range of the central region $R_{0.5}^{(j)}(t)$ times the sparseness proportion $p_s^{(j)}(t)$ from the upper bound of $C_{0.5}^{(j)}(t)$ at each time index t . Then, we display this percentage with a smoothed $l^{(j)}(t, p_s^{(j)}(t))$ over $\widetilde{\mathcal{T}}$ showing the observed proportion below and the sparseness proportion above. We fill the observed proportion area in magenta and the sparseness proportion area in gray. In addition, we plot a thin dotted cyan reference line, $l^{(j)}(t, 0.5)$, to represent the case of $p_s^{(j)}(t) = 0.5$ for all $t \in \widetilde{\mathcal{T}}$. For the detected outliers, the fitted missing values are represented by dashed gray, whereas the observed values are marked with dashed red.

3.2. Intensity Sparse Functional Boxplot

The sparse functional boxplot provides information about the sparse point proportion at each time, but we do not know the distribution of sparse points within the central region. To give a pattern of the intensity of sparse points, we construct the intensity sparse functional boxplot.

In addition to the aforementioned characteristics of the functional boxplot, we display the intensity of fitted missing point patterns within the 50% central region $C_{0.5}^{(j)}$, for any j th ($j = 1, \dots, p$) component. Assuming that we have altogether S original missing point data within $C_{0.5}^{(j)}$, we regard the fitted sparse points within $C_{0.5}^{(j)}$ as a spatial point pattern $\mathbf{u}_s^{(j)} := \{(t_s, Z_s^{(j)}) \in C_{0.5}^{(j)}, s = 1, \dots, S\}$ with t_s the time, and $Z_s^{(j)}$ the fitted value inside the central region. Then we compute a kernel smoothed intensity function ([Diggle 1985](#)) from the point pattern. The intensity estimate is corrected by dividing it by the convolution of the Gaussian kernel with the observation window. Thus, the sparseness intensity at a new point $\mathbf{u}^{(j)} \in C_{0.5}^{(j)}$ is

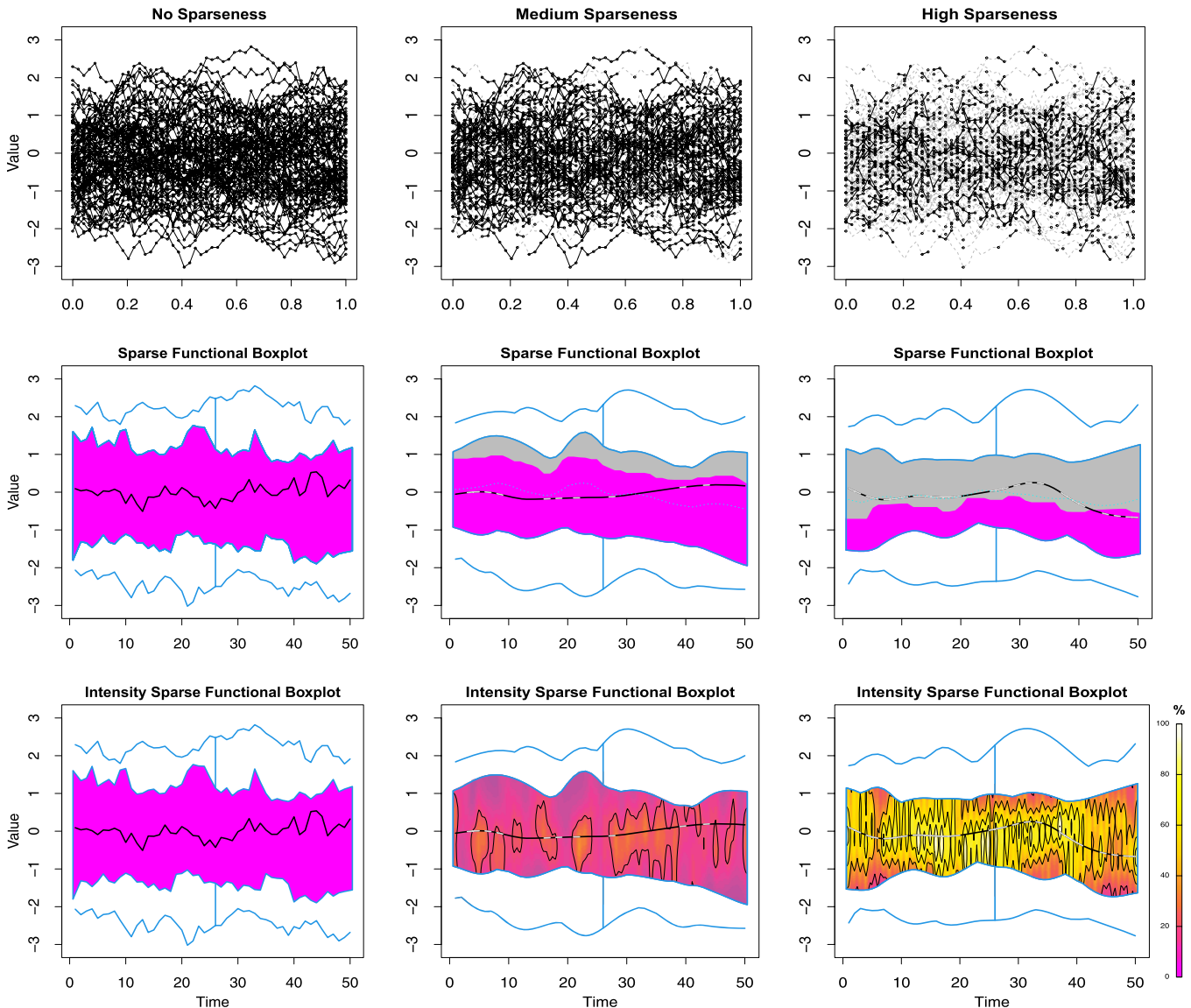


Figure 3. The first row displays the univariate functional data from a Gaussian process with mean zero and exponential covariance function $C(t,s) = \exp\{-|t-s|\}$, with the corresponding sparse functional boxplots on the second-row and the corresponding intensity sparse functional boxplots on the third-row. Plots from left to right display three sparseness cases: No sparseness, medium sparseness (on average 20% values are missing in each curve), and high sparseness (on average 60% values are missing in each curve).

$$\lambda(\mathbf{u}^{(j)}) = e(\mathbf{u}^{(j)}) \sum_{s=1}^S w_s \mathcal{K}(\mathbf{u}_s^{(j)} - \mathbf{u}^{(j)}), \quad (6)$$

where \mathcal{K} is the Gaussian smoothing kernel, $e(\mathbf{u}^{(j)})$ is an edge correction factor, and w_s are the weights. The computation of such intensity is available in the R package *spatstat.core* (Baddeley et al. 2022). By default, the intensity values of fitted sparse point patterns are expressed in estimated missing points per unit area.

Then, we normalize $\lambda(\mathbf{u}^{(j)})$ to $\lambda_{\text{norm}}(\mathbf{u}^{(j)}) := \frac{\lambda(\mathbf{u}^{(j)})}{\max_{\mathbf{u}_s^{(j)}} \{\lambda(\mathbf{u}_s^{(j)})\}}$. To

visualize the change of the relative intensity, we use a color scale between magenta for the case of zero intensity within the central region ($\lambda_{\text{norm}}(\mathbf{u}^{(j)}) = 0$), and white for the case of maximal intensity within the central region ($\lambda_{\text{norm}}(\mathbf{u}^{(j)}) = 1$). Furthermore, we can divide the intensity $\lambda(\mathbf{u}^{(j)})$ by the maximum among all variables j if one wants to compare the relative

intensity among variables. We also leave an option of whether contours of the sparseness intensity are shown in the central region.

To illustrate the visualization tools, we generate univariate functional data without outliers through a Gaussian process with zero mean and exponential covariance $C(t,s) = \exp\{-|t-s|\}$. Here we normalize the sparseness intensity by dividing it by the maximum sparseness intensity across all sparseness levels. The first row in Figure 3 displays settings of no sparseness, medium sparseness, and high sparseness, with the corresponding sparse functional boxplots on the second-row and the corresponding intensity sparse functional boxplots on the third-row. Here, medium sparseness implies around 20% missing values in every curve, whereas high sparseness implies around 60% missing values in every curve. The magenta and gray colors in the sparse functional boxplot represent the proportion of observed values and missing values within the central region. Correspondingly, in the intensity sparse functional boxplot, the

magenta color means zero sparseness intensity, the tomato color means 25% of the maximum sparseness intensity, the gold color means 50% of the maximum sparseness intensity, the yellow color means 75% of the maximum sparseness intensity, and the white color means the maximum 100% sparseness intensity.

When the data are complete, the sparse and intensity sparse functional boxplots (first column, Figure 3) reduce to the original functional boxplot. When the sparseness level increases, the sparse functional boxplot (second row, Figure 3) changes from no gray area to almost a 20% gray area, and then nearly 60% gray area in proportion to the central region, reflecting the change of the missing proportion per time index. Simultaneously, we observe that the sparseness intensity (third row, Figure 3) within the central region generally increases with the increase of sparseness, which can be seen from the corresponding color change from the all-over magenta to tomato and magenta, and finally to mainly gold, yellow, and few white.

Given an intensity sparse functional boxplot, we can find the area with the most and least relative sparseness intensities and compare the relative sparseness intensity at any fixed time within the central region. Taking the bottom right intensity sparse functional boxplot as an example, we see the area with the time index between 5 and 40 and the value between -1 and 0.2 is labeled in yellow, which indicates at least 75% of the maximum sparseness intensity in this area. In contrast, the area close to the envelopes of the central region is colored with gold and tomato, which indicates 25%–50% of the maximum sparseness intensity. On the other hand, the central region in the bottom middle intensity sparse functional boxplot is mainly colored in magenta and tomato, which indicates the sparseness intensity is smaller than 25% of the maximal sparseness intensity. In addition, the bottom middle intensity sparse functional boxplot displays that the fitted sparse values mainly concentrate on the tomato region.

3.3. Sparse Two-Stage Visualization Tools

Similar to the generalization of the two-stage functional boxplot (Dai and Genton 2018a) from the functional boxplot, the sparse two-stage functional boxplot and intensity sparse two-stage functional boxplot can be easily proposed by implementing the directional outlyingness (Dai and Genton 2019).

Consider a p -variate stochastic process $\{\mathbf{X}(t), t \in \tilde{\mathcal{T}}\}$ on \mathbb{R}^p with at each time point t cdf $F_{\mathbf{X}(t)}$ that generates continuous paths on $C^p(\tilde{\mathcal{T}})$. Take an arbitrary $\mathbf{Z} \in C^p(\tilde{\mathcal{T}})$. Then $\mathbf{Z}(t)$ is a random vector on \mathbb{R}^p . These aforementioned authors first defined the outlyingness $\mathbf{O}(\mathbf{Z}(t), F_{\mathbf{X}(t)}) = \{1/D(\mathbf{Z}(t), F_{\mathbf{X}(t)}) - 1\} \cdot \mathbf{v}$, where D is a statistical depth function from \mathbb{R}^p , and \mathbf{v} is the unit vector pointing from the median of $F_{\mathbf{X}(t)}$ to $\mathbf{Z}(t)$. Then, they proposed the magnitude outlyingness and shape outlyingness: $\mathbf{MO}(\mathbf{Z}, F_{\mathbf{X}}) := \int_{\tilde{\mathcal{T}}} \mathbf{O}(\mathbf{Z}(t), F_{\mathbf{X}(t)}) dt \in \mathbb{R}^p$ and $\mathbf{VO}(\mathbf{Z}, F_{\mathbf{X}}) := \int_{\tilde{\mathcal{T}}} \{\mathbf{O}(\mathbf{Z}(t), F_{\mathbf{X}(t)}) - \mathbf{MO}(\mathbf{Z}, F_{\mathbf{X}})\}^\top \{\mathbf{O}(\mathbf{Z}(t), F_{\mathbf{X}(t)}) - \mathbf{MO}(\mathbf{Z}, F_{\mathbf{X}})\} dt \in \mathbb{R}$. Here \mathbf{MO} and \mathbf{VO} are used to measure the magnitude and shape outlyingness of a curve.

A robust Mahalanobis distance (RMD, Rousseeuw 1984) is calculated between all $(\mathbf{MO}_i, \mathbf{VO}_i)^\top \in \mathbb{R}^{p+1}$ ($i = 1, \dots, N$) and its mean vector obtained from the minimal covariance

determinant (Rousseeuw and Van Driessen 1999). Then, a curve \mathbf{Z}_o is recognized as an outlier if its $(\mathbf{MO}_o, \mathbf{VO}_o)^\top$ satisfies $\text{RMD}_{(\mathbf{MO}_o, \mathbf{VO}_o)^\top}^2 \geq C_{\text{RMD}, \alpha_f}$. Here, C_{RMD, α_f} is the $(1 - \alpha_f)$ th percentile of Fisher's F distribution, F_{RMD} (Hardin and Rocke 2005), and α_f is the significance level.

With the directional outlyingness, we can improve the robustness of the sparse functional boxplot in a two-stage procedure. First, we obtain the set of outliers by applying directional outlyingness to the fitted data. Then, we apply the sparse functional boxplot procedure to the remaining curves. We add the detected outlying curves from stage one, with green color labeling the observed points, and gray color labeling the missing points.

Overall, when combined, the sparse functional boxplot and the intensity sparse functional boxplot provide information about the proportion and intensity of sparse points within the central regions. The choice between the sparse functional boxplot and the sparse two-stage functional boxplot depends on the existence of outliers in the data. When no outliers exist, there is no difference between the sparse functional boxplot and the sparse two-stage functional boxplot. Specifically, the simulation in Section 4.3 explores performances of the sparse functional boxplot and its two-stage form when detecting multivariate functional outliers.

4. Simulation Study

This section starts with an introduction of the data settings and a discussion of sparseness. Next, we address two problems in the simulations: first, we explore the choice of the best depth; second, we evaluate the outlier detection performances of the sparse functional boxplot and the sparse two-stage functional boxplot with the best depth.

4.1. Simulation Settings

For simplicity, we assume $p = 3$. The complete data are defined on common time grids. Then we assign the point, peak, and partial sparseness to variables 1–3 in the simulations. We set $N = 100$, and the common times are from 50 equidistant points in $[0, 1]$. We use $\mu(t) = (5 \sin(2\pi t), 5 \cos(2\pi t), 5(t - 1)^2)^\top$, $\epsilon_i(t) \stackrel{\text{iid}}{\sim} \mathcal{N}_3(\mathbf{0}, \text{diag}\{\sigma_1^2, \sigma_2^2, \sigma_3^2\})$. Here, $\sigma_1^2, \sigma_2^2, \sigma_3^2$ are independent and follow $U[0.3, 0.5]$, where U means a random sampling from the uniform distribution. We use orthonormal Fourier basis functions to construct $\psi_m^{(j)}(t)$. We let $M = 9$, $\rho_{i,m} \stackrel{\text{iid}}{\sim} \mathcal{N}(0, v_m)$, and $v_m = \frac{M+1-m}{M}$.

Eight models are provided by specifying the eigenfunctions and outliers as below. Model 1 is a reference model without contamination, while the remaining models include contamination by adjusting $\mu(t)$, $\mathbf{u}_i(t)$, or $\epsilon_i(t)$, with a contamination level of 10%. Models 2–4 introduce magnitude outliers (Sun and Genton 2011), and Models 5–8 generate shape outliers (Dai and Genton 2018b, Dai and Genton 2019).

Model 1 (no outlier): $\mathbf{Y}_i(t) = \mu(t) + \mathbf{u}_i(t) + \epsilon_i(t) = \mu(t) + \sum_{m=1}^M \rho_{i,m} \psi_m^{(j)}(t) + \epsilon_i(t)$, $i = 1, \dots, N$.

Model 2 (persistent magnitude outliers): $\mathbf{u}_{i,\text{ou}}^{(j)}(t) = \mathbf{u}_i^{(j)}(t) + 8w_{i,j}$ for $t \in [0, 1]$, where $w_{i,j}$ ($j = 1, 2, 3$) follows the binomial

distribution of obtaining 1 with probability 0.5, and -1 with probability 0.5 and all w_{ij} s in the manuscript follow the same distribution as in Model 2.

Model 3 (isolated magnitude outliers): $u_{i,ou}^{(j)}(t) = u_i^{(j)}(t) + 8w_{ij}$ for $t \in [T_s, T_s + 0.1]$, and T_s is from $U[0, 0.9]$.

Model 4 (shape outliers I): $\mu_{ou}(t) = (\mu^{(1)}(t - 0.3), \mu^{(2)}(t - 0.2), \mu^{(3)}(t - 0.5))^\top$.

Model 5 (shape outliers II): $u_{i,ou}^{(1)}(t) = u_i^{(1)}(t) + 2 \sin(4\pi t)$, $u_{i,ou}^{(2)}(t) = u_i^{(2)}(t) + 2 \cos(4\pi t)$, $u_{i,ou}^{(3)}(t) = u_i^{(3)}(t) + 2 \cos(8\pi t)$, $u_{i,no}^{(j)}(t) = u_i^{(j)}(t) + U_j$, $j = 1, 2, 3$, where U_j is generated from $U[-2.1, 2.1]$.

Model 6 (mixed outliers): $\mu_{i,ou}(t) = ((2 + R_i^{(1)})\mu^{(1)}(t), (2 + R_i^{(2)})\mu^{(2)}(t), (2 + R_i^{(3)})\mu^{(3)}(t) - 6)^\top$, $j = 1, 2, 3$, where $R_i^{(j)}$ follows $\text{Exp}(2)$, and Exp is a random sampling from the exponential distribution.

Model 7 (joint outliers): $u_{i,ou}^{(1)}(t) = Z_1 t \sin(\pi t)$, $u_{i,ou}^{(2)}(t) = Z_2 t \cos(\pi t)$, $u_{i,ou}^{(3)}(t) = Z_3 t \sin(2\pi t)$, $u_{i,no}^{(1)}(t) = Z_4 t \sin(\pi t)$, $u_{i,no}^{(2)}(t) = (8 - Z_4)t \cos(\pi t)$, $u_{i,no}^{(3)}(t) = (Z_4 - 2)t \sin(2\pi t)$, where Z_1-Z_4 are generated from $U[2, 8]$.

Model 8 (covariance outliers): $\epsilon_i(t)$ are generated from a stationary isotropic cross-covariance model belonging to the Matérn family (Gneiting, Kleiber, and Schlather 2010) with smoothness parameters $v_{ij} > 0$: $C_{ii}(s, t) = \sigma_i^2 \mathcal{M}(|s - t|; v_{ii})$ for $i = 1, 2, 3$, and $C_{ij}(s, t) = \rho_{ij}\sigma_i\sigma_j \mathcal{M}(|s - t|; v_{ij})$ for $1 \leq i < j \leq 3$, and $\mathcal{M}(r; v_{ij}) = \frac{2^{1-v_{ij}}}{\Gamma(v_{ij})} (\sqrt{2v_{ij}}r)^{v_{ij}} K_{v_{ij}}(\sqrt{2v_{ij}}r)$, where K_v is the modified Bessel function of the second kind of order v , v_{ii} is generated from the uniform distribution, with ranges $[2, 3]$ for the nonoutliers and $[0.1, 0.2]$ for the outliers, $v_{ij} = \frac{v_{ii}+v_{jj}}{2}$, $\rho_{ii} = 1$, and $\rho_{ij} = \frac{i+j}{i+j+3}$.

To categorize possible sparseness scenarios, we consider three sparseness types in marginal functional data: point, peak, and partial sparseness. Point sparseness means that missing points appear randomly in time grids, and the location and number of missing points are independent per curve. The peak and partial sparseness mean that values are missing during a continuous interval starting from a random point t_{start} . The difference between peak and partial sparseness lies in the t_{start} . In the peak sparseness, for each curve, t_{start} is generated independently, while in the partial sparseness, all curves with missing values share a common t_{start} . Define p_{size} (the number of curves with missing values divided by the total number of curves) as the probability of a curve with at least one missing value in all sample curves, and p_{curve} (the number of missing points in the curve divided by the number of complete-time measurements in the curve) as the probability of sparseness in each of those curves with missing values. Hence, we use the sparseness parameter $\mathbf{p}_s = (p_{\text{size}}, p_{\text{curve}}, t_{\text{start}})^\top$ to tune the sparseness.

It is worth noting that t_{start} is only required in the peak and partial sparseness as a starting point of the missing interval. Here, t_{start} is a realization from $U[0, 1 - p_{\text{curve}}]$. Usually, the missing interval does not cover the first or the last time point in $[0, 1]$. Otherwise, it is difficult for BMFPCA to reconstruct curves with suitable fittings unless the curves follow simple monotone trends, such as for the data application in Section 5.2.

We display a simulation for Models 1, 2, 4 (Figure 4) to illustrate the sparseness types and \mathbf{p}_s , while the remaining simulation visualizations are shown in the [supplementary material](#). In Figure 4, variables 1–3 belong to the point (first column), peak (second column), and partial (third column) sparseness types, respectively, with $N = 100$ and contamination level 10%. Here, $p_{\text{size}} = 100\%$ means that 100 curves from the simulation contain missing values, and $p_{\text{curve}} = 40\%$ means that in each curve with missing values, there are about 20 time measurements with missing values given 50 time measurements. We can see that each curve has different missing time points per curve in the point sparseness (first column, Figure 4). In addition, we also observe a missing interval with the various start of missing points per curve (second column, Figure 4) in the peak sparseness, and a missing interval with a common start of missing points (third column, Figure 4) in the partial sparseness.

4.2. Simulation I: Choice of Depth

We apply the conventional depth to the MFPCA and BMFPCA fits (Equations (1)–(2)), and name them $\text{MFHD}_{\text{mfPCA}}$ and $\text{MFHD}_{\text{bmfpca}}$, respectively. We set $B = 100$ in the BMFPCA fit. The BMFPCA fit is more robust and closer to the original data than the MFPCA fit. Hence, we apply the remaining revised depths RMFHDAw and RMFDNaw (Equation (5)) to the BMFPCA fit.

The Spearman rank correlation coefficient (Kendall 1945) assesses how well the rank based on the fitted data, given by the revised depth, correctly associates with the rank based on the original complete data, given by the conventional depth. When the coefficient is closer to 1, the stronger the association, and when it is closer to 0, the weaker the association.

The Spearman coefficients of the above four methods are presented in Figure 5 under various p_{curve} with $p_{\text{size}} = 100\%$ for Models 1, 2, and 4 when the point sparseness exists in all variables. The results of the remaining models from the point sparseness and those from other sparseness types can be seen in the [supplementary materials](#). All depths show a bit of weaker association when the curve is sparser on average in the peak and partial sparseness types. Generally, the application of MFHD to the BMFPCA has a stronger rank association than the application of MFHD to the MFPCA with the original data and have a slight advantage over the revised depth MFHD_{aw} and MFHD_{naw} .

Overall, $\text{MFHD}_{\text{bmfpca}}$ provides excellent performance with its strong rank associated with the original data and simple procedure of application for sparse multivariate functional data. It omits the confidence band construction and thus, requires no additional depth modifications and is more efficient in computation.

4.3. Simulation II: Choice of Visualization Tools

We apply the sparse functional boxplot and the sparse two-stage functional boxplot in different scenarios with $\text{MFHD}_{\text{bmfpca}}$. The two-stage functional boxplot detects both magnitude and shape outliers with the help of directional outlyingness. We use p_c , the

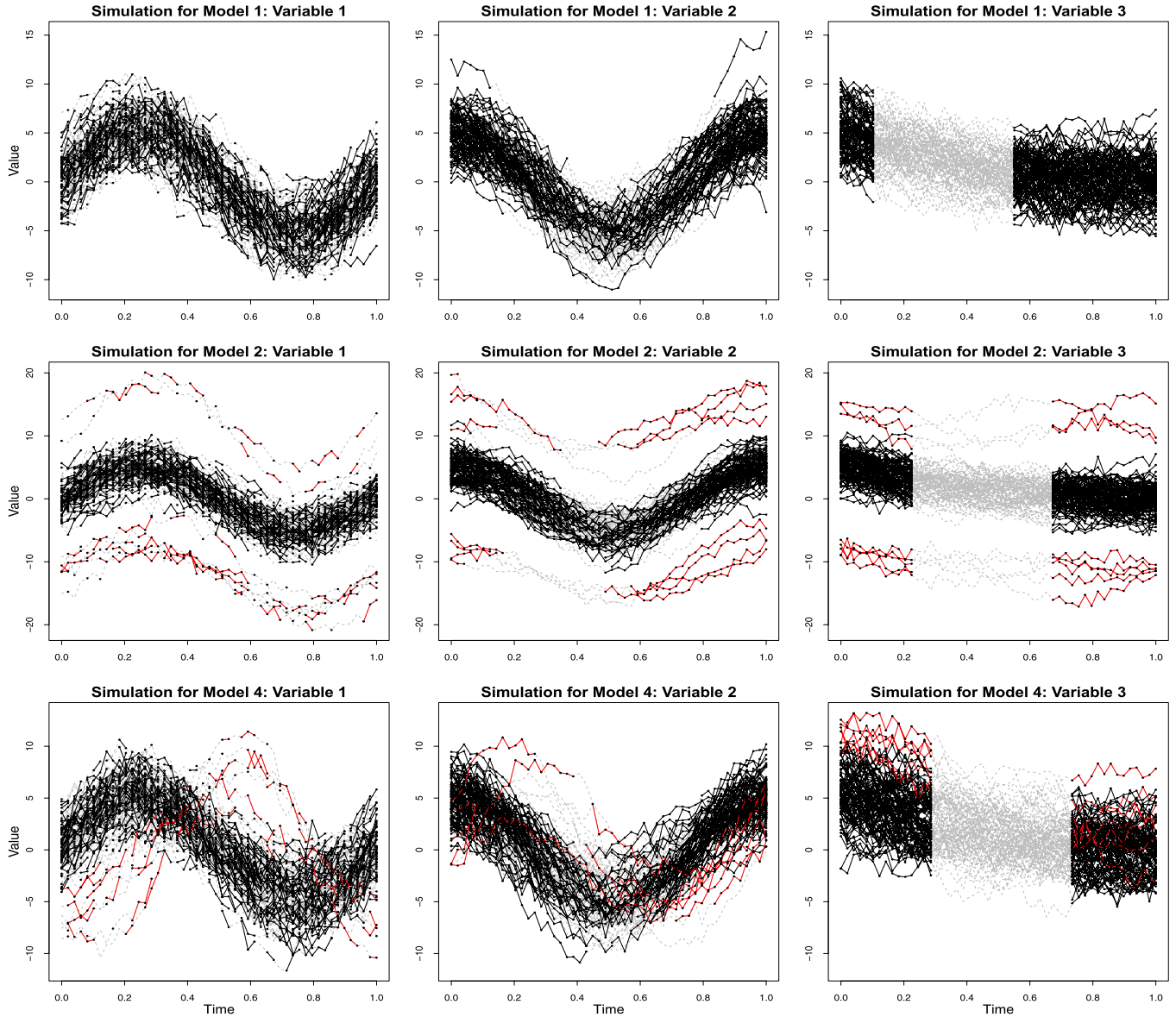


Figure 4. Simulations for Models 1 (no outlier), 2 (persistent magnitude outliers), and 4 (shape outliers I), with $p_{curve} = 40\%$ and $p_{size} = 100\%$. Typical curves are colored in black in the simulation plot, and outliers are colored in red, with the observed points shown as black dots. Artificial sparseness is represented by gray dashed lines. We assign the point, peak, and partial sparseness to variables 1, 2, and 3 in the simulation.

correct detection rate (the number of correctly detected outliers divided by the number of outliers) and p_f , the false detection rate (the number of falsely detected outliers divided by the number of nonoutliers) to measure the performance of the above two tools in multivariate functional outlier detection.

We display in Table 1 the performance of p_c and p_f for Models 2 and 4 when the point sparseness is assigned to all variables, while the other performances are provided in the [supplementary materials](#). Overall, the sparse two-stage functional boxplot performs better in detecting true outliers than the sparse functional boxplot, at the expense of a slightly higher p_f .

BMFPCA fits the curves after removing the mean trend; hence, it manages to capture the typical behavior of the curves independently of their amplitude. Suppose outliers show an abnormality, especially in the shifted amplitude or time. In that case, the sparse two-stage functional boxplot obtains a high p_c , see Models 2 (persistent magnitude outliers) and 4 (shape outliers I). We see a somewhat smaller p_c , between 50% and

80%, from the sparse two-stage functional boxplot in Models 3 (isolated magnitude outliers), 6 (mixed outliers), and 7 (joint outliers), where the abnormality mainly appears in an interval of the outliers. Furthermore, we notice that the sparse two-stage functional boxplot does not detect outliers well in Models 5 (shape outliers II) and 8 (covariance outliers), showing a smoothness difference between abnormal and normal curves. It is difficult to detect the outlying samples due to not many smoothness differences among the fitted curves. On the whole, we recommend the sparse two-stage functional boxplot for detecting potential outliers.

5. Applications

Applications include the univariate CD4 cell counts and bivariate malnutrition data introduced in Section 1. The analysis follows the procedures of fitting the data and consideration between the sparse functional boxplot and its two-stage form.

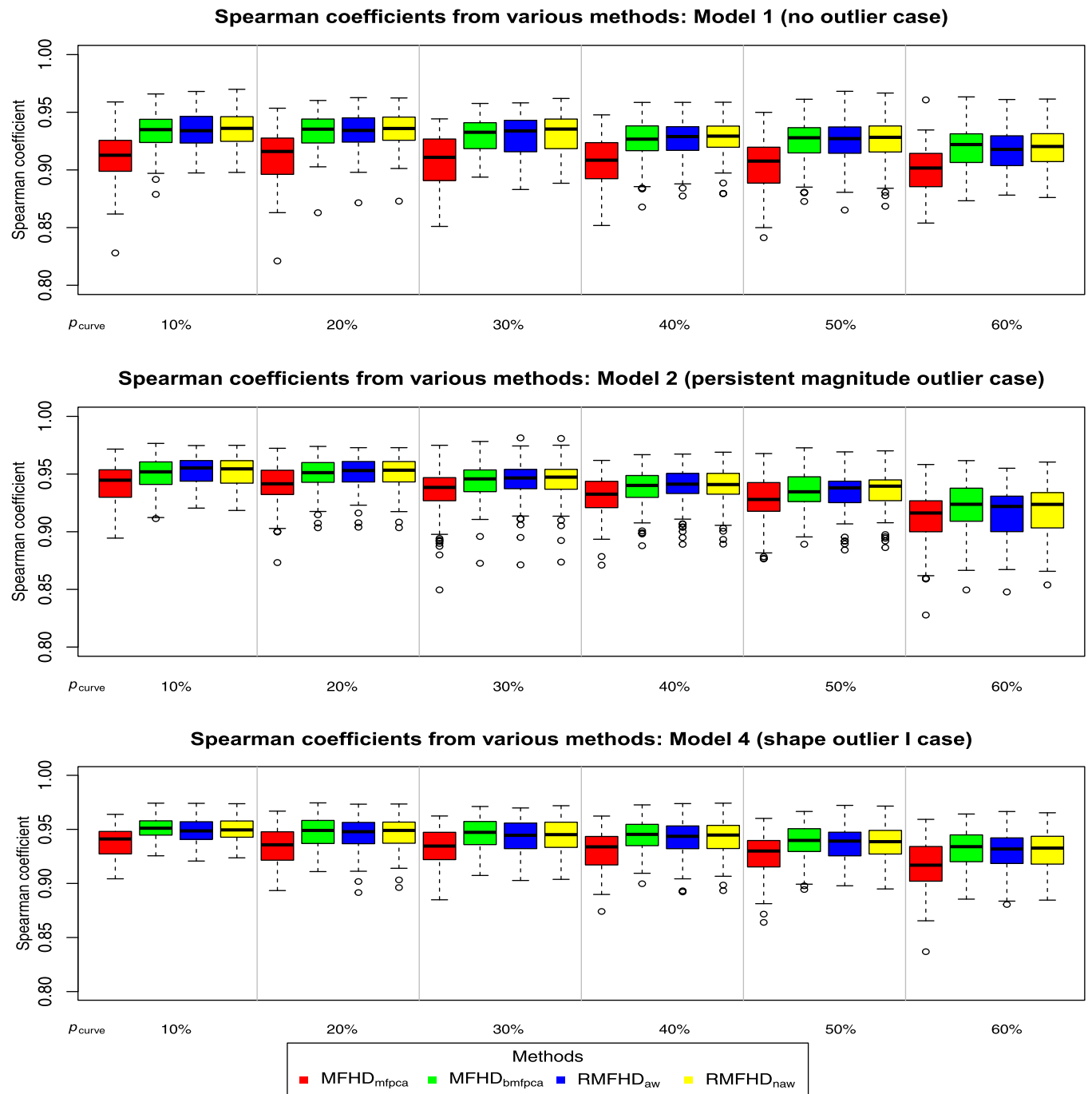


Figure 5. Comparison of four depth ranking methods for Models 1, 2, and 4. The panels from top to bottom represent boxplots of Spearman coefficients under various data settings. In each setting, p_{curve} is given from 10% to 60%, with $p_{\text{size}} = 100\%$ in the point sparseness type. The number of replicates is 100.

Table 1. The mean and standard deviation (in parenthesis) of the percentages p_c and p_f for the sparse functional boxplot and the sparse two-stage functional boxplot with 100 replications and 100 curves when the curve sparseness p_{curve} is 20%, 40%, and 60%, respectively, and $p_{\text{size}} = 100\%$ for the point sparseness type, in the presence of Models 2 (persistent magnitude outliers) and 4 (shape outliers I).

Curve sparseness	$p_{\text{curve}} = 20\%$		$p_{\text{curve}} = 40\%$		$p_{\text{curve}} = 60\%$	
Methods \ Ratios	p_c	p_f	p_c	p_f	p_c	p_f
Sparse: Model 2	64.9 (25.0)	0.0 (0.0)	61.4 (23.5)	0.0 (0.0)	66.0 (25.5)	0.0 (0.0)
Sparse: Model 4	15.7 (19.4)	0.0 (0.0)	15.4 (21.4)	0.0 (0.0)	13.5 (19.4)	0.0 (0.0)
Sparse Two-stage: Model 2	100.0 (0.0)	0.0 (0.0)	100.0 (0.0)	0.0 (0.0)	100.0 (0.0)	0.0 (0.0)
Sparse Two-stage: Model 4	97.8 (4.9)	0.1 (0.5)	97.1 (6.3)	0.1 (0.4)	97.5 (4.8)	0.1 (0.4)

NOTE: The probability of outliers in each model is 10%.

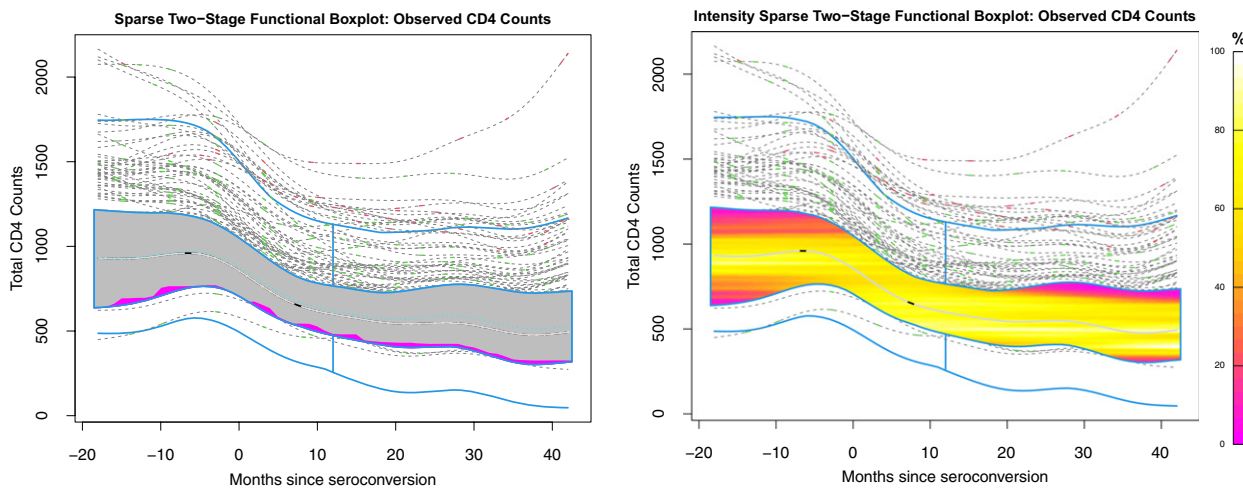


Figure 6. The sparse two-stage functional boxplot and the intensity sparse two-stage functional boxplot for observed CD4 cell counts. Seventy-eight outliers (green dashes) are detected from directional outlyingness, and eight outliers (red dashes) are detected from the functional boxplot.

We do not show contours in the intensity sparse two-stage functional boxplot for the CD4 cell counts due to the narrow range in the central region, but we offer them for the malnutrition data.

5.1. Univariate Case: CD4 Cell Counts Data

The human immune deficiency virus (HIV) harms the body by attacking an immune cell called the CD4 cell and, thus, making the body more vulnerable to other illness-causing germs. Hence, CD4 cell count per milliliter of blood (Taylor et al. 1989) can be used to track the progression of HIV. A person with untreated HIV will experience a series of stages: acute HIV infection (2–6 weeks), stage one (1–5 years), stage two (6–9 years), stage three (9–11 years), which is advanced HIV disease, and stage four (11–12 years), which is called the acquired immunodeficiency syndrome (AIDS). In the acute HIV infection and in stage one, the CD4 cell count drops slowly and is usually above 500; during stage two, it ranges between 350 and 499. In the stage three, the CD4 count is 200–349, whereas in the stage four the CD4 count is less than 200 (HIV.gov 2020). These CD4 cell counts data are available in the *refund* package (Crainiceanu and Goldsmith 2010) in R and were analyzed by Goldsmith, Greven, and Crainiceanu (2013) to construct the bootstrap improved confidence bands for sparse functional data. It includes observed CD4 cell counts for 366 infected individuals from −18 to 42 months (Figure 1), where 0 represents seroconversion, the moment when the antibody becomes detectable in the blood. The observation period in this dataset includes acute HIV infection and stage one, or stage two for some patients who are in worse situations.

Figure 6 contains the CD4 cell counts after they were fitted with the iterated expectation from UFPCA, and ordered according to the modified band depth (MBD, López-Pintado and Romo 2009). Compared to the original sparse observations shown in Figure 1, the fit ranges between 20 and 2173, which lies in the field of low and normal CD4 cell count per cubic millimeter of blood. The CD4 cell count is a point sparseness case with $p_{size} = 100.0\%$ and p_{curve} is between 82.0% (11 observations per subject) and 98.4% (1 observation), which is displayed by the magenta area in the sparse two-stage functional boxplot in Figure 6. The sparse functional boxplot detects seven outliers with a contamination level of 3.0%. The sparse two-stage

functional boxplot detects 78 outliers (green dashed lines) from directional outlyingness and eight extra outliers (red dashed lines) from the functional boxplot, with a contamination level of 23.0%. Additionally, the intensity sparse two-stage functional boxplot indicates that gold and yellow colors fill most central parts within the central region, which correspond to 50%–75% of the maximal sparseness intensity. Conversely, the region with small sparseness intensity mainly lies in the magenta areas, one at the start when the CD4 estimated counts are below 700 and above 1200, and another between 20 and 42 months after seroconversion when the CD4 cell counts are below 400 and above 800.

The 50% central region starts between 631 and 1497 at 18 months before seroconversion and ends between 316 and 744 at 42 months after seroconversion. The median shows a change in CD4 cell counts from 935 to 500 during the observation period. There are 27.5% of patients who show CD4 cell counts below 350 at 42 months after seroconversion, implying that they are close to, or already at, stage three. However, 89.5% of outliers show a rising trend of CD4 cell counts above 500 in the period after seroconversion, suggesting that they are on the right track against HIV.

In this analysis, we wish to review the progression of an HIV infection during different observation periods according to the visualization tools we introduced. In the window period, before the HIV antibody can be detected in the blood, CD4 cell counts have an inverse U shape, which can be seen from outliers and the upper fence of the central region (Figure 6) between 10 months before and 10 months after the seroconversion, implying the process of rapid replication and severe drop in CD4 cells. This reflects the HIV first invading the body, stimulating CD4 cells to replicate, and then infecting CD4 cells by injecting them with its genetic material, leading to a fast drop in the number of CD4 cells. Surprisingly, there are 21 patients with CD4 cell counts around or above 1000 at 42 months after seroconversion, whose treatment or lifestyle may deserve further study.

5.2. Bivariate Case: Malnutrition Data

The malnutrition data, from the United Nations Children's Fund (UNICEF 2020) data warehouse, include two variables, stunted growth and the prevalence of low birth weight, collected in

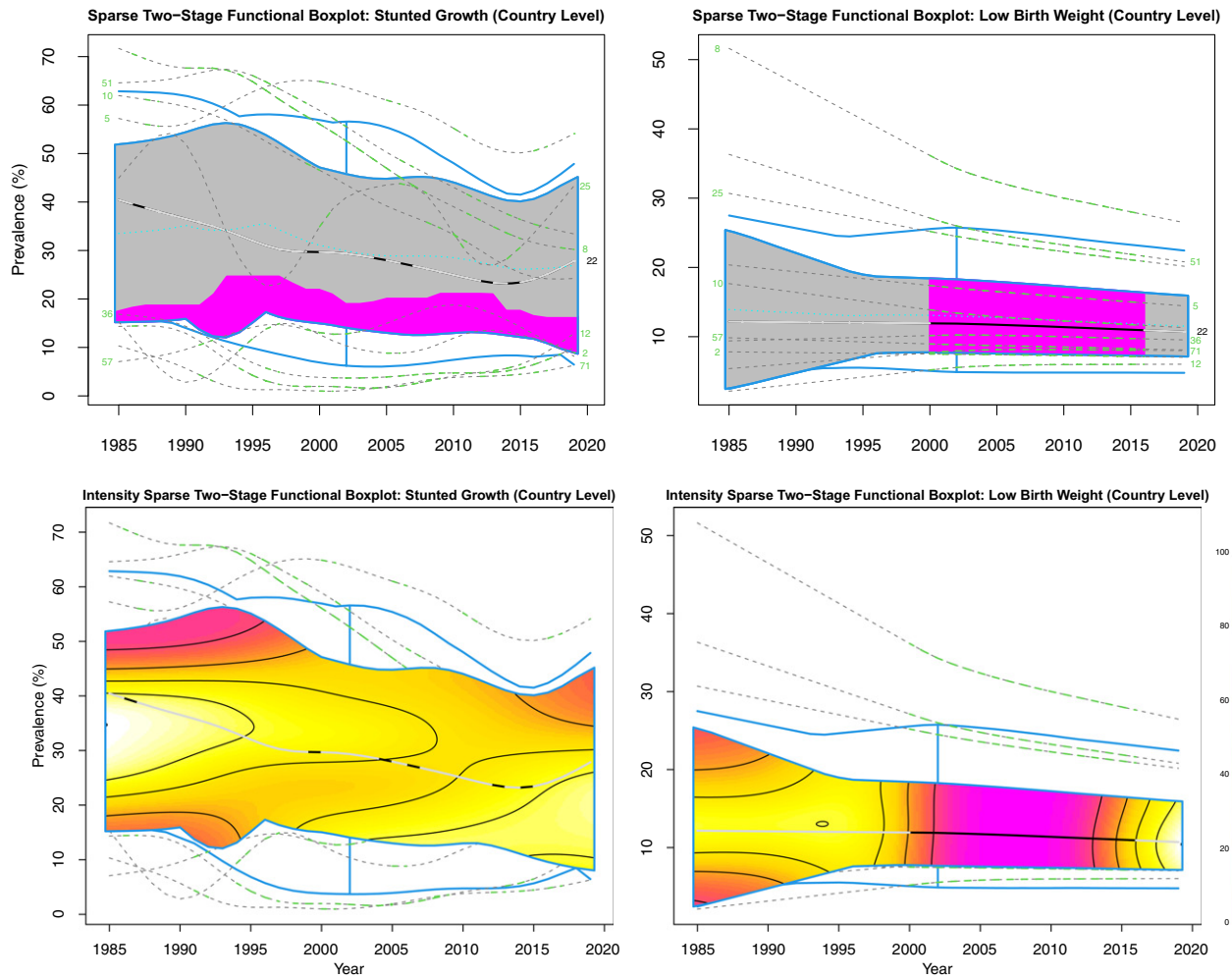


Figure 7. Visualization of stunted growth and low birth weight data for 77 countries with the sparse two-stage functional boxplot and the intensity sparse two-stage functional boxplot. One-to-one maps (number, outlier/median nation) are the following: (2, Argentina), (5, Burundi), (8, Bangladesh), (10, Bhutan), (12, Chile), (22, Ecuador), (25, Guinea-Bissau), (36, Kuwait), (51, Nepal), (57, Romania), and (71, United States).

77 countries from 1985 to 2019. Stunted growth is defined as the proportion of newborns aging from 0 to 59 months with a low height-for-age measurement (below two standard deviations). The stunted growth data represent a point sparseness case with 4–23 recordings per nation; p_{curve} ranges from 29.4% in Bangladesh to 88.2% in Argentina. The low birth weight data are a partial sparseness case, with recordings during 2000–2015 only; $p_{\text{curve}} = 52.9\%$ for all nations.

Since only one outlier (Bangladesh) is detected as a magnitude outlier in the prevalence of the low birth weight via the sparse functional boxplot, we implemented the sparse two-stage functional boxplot and detected 10 outliers. First, the gray and magenta in the central region (top row of Figure 7) display the sparseness proportion of the central region for each variable. In addition, the median and fences of the central region display that most nations went through a significant decline in stunted growth prevalence over time, while most countries had a slow drop or rise before 2000 and a steady trend since 2000 in low birth weight. Furthermore, the low birth weight prevalence is right-skewed which can be seen from the margin difference between the central region and the fences. The skewed setting suggests more attention to nations with high prevalence of low birth weight is needed.

The intensity sparse two-stage functional boxplot (bottom row, Figure 7) displays the relative intensity of the fitted missing values inside the central region for each variable. The missing values for the prevalence of low birth weight are most intense in the almost white region: with the interval 1985–1988 and the estimates around 30%–40%. Comparatively, the missing values with the most intensity for the low birth weight lie in the region where the estimates are between 8% and 12% and time is between 2018–2019. In addition, we can see the relative intensity of fitted missing values in both variables at each fixed time. For instance, for the stunted growth, when the year is 1985, missing values are mostly distributed between 25% and 40% prevalence labeled in white, followed by the prevalence between 21%–25% and 40%–42% labeled in yellow, after that the prevalence between 19%–21% and 42%–44% labeled in gold, then the prevalence between 16%–19% and 45%–49% labeled in tomato, succeeded by the prevalence above 49% including the least sparseness intensity labeled in magenta.

We use the human development index (United Nations Development Programme 2019), which categorizes countries into low, medium, high, and very high human development groups, to analyze the malnutrition trend in these countries. In the last 35 years, the median, Ecuador, shows a representative

trend of a smooth decline from 40% to 24% in the prevalence of stunted growth, and a constant trend around 12% in the prevalence of low birth weight. Outliers exist in almost all human development groups, often showing an abnormality in the shape of stunted growth prevalence. From the very high human development group, Argentina, Chile, Kuwait, Romania, and the United States demonstrate an exception in shape lying at the bottom of the stunted growth's prevalence and a slow rise at the bottom of the low birth weight's prevalence. From the middle human development group, Bhutan shows only an abnormal shape in the prevalence of stunted growth, which is not far from their respective median. Finally, Bangladesh, Burundi, Guinea-Bissau, and Nepal, which all belong to the low human development index group, lie at the top of the samples in Figure 7. They all show a faster decline rate in the prevalence of the stunted growth compared to the rest of their group and a significant decline, especially for Bangladesh and Nepal, in the prevalence of the low birth weight. Nevertheless, they are on top of the curves in 2019 and need more actions to reduce malnutrition.

6. Discussion

In this article, we proposed two flexible tools, the sparse functional boxplot and the intensity sparse functional boxplot, for visualizing sparse multivariate functional data. We also introduced a sparse form of the two-stage functional boxplot (Dai and Genton 2018a), which is itself a derivation from the functional boxplot (Sun and Genton 2011) with better outlier detection. All of these can be applied in both univariate and multivariate functional settings. When the data are observed on common time grids without missing values, the tools reduce to the original functional boxplot and two-stage functional boxplot. We believe the introduction of visualization tools for sparse data is of great importance due to the wide applications of longitudinal studies and the common challenge of missing values in real datasets.

To apply the visualization tools described above to sparse functional data, an appropriate data fitting and depth for data ordering is required. In addition to the novel contribution in the sparse and intensity sparse functional boxplot, we improved the fitting of data (MFPCA, Happ and Greven 2018) through the iterated expectation from bootstrap (Goldsmith, Greven, and Crainiceanu 2013), and investigated several depths for sparse multivariate functional data. Here, we took the multivariate functional halfspace depth (MFHD, Claeskens et al. 2014) as a building block for proposing various revised depths for sparse multivariate functional data. We obtained the best depth via the Spearman rank coefficient simulated in various data settings and sparseness scenarios. In the univariate functional setting, MFPCA became UFPCA (Yao, Müller, and Wang 2005), and we used the modified band depth (MBD, López-Pintado and Romo 2009) to order the data, prior to the application of visualization tools.

Besides data visualization, the sparse functional boxplot and its two-stage form can also detect outliers. Simulations demonstrated that generally, the sparse two-stage functional boxplot performed better than the sparse functional boxplot in outlier detection. In some shape outlier cases, the advantage of outlier detection from directional outlyingness (Dai and Genton 2019)

is not obvious, and may require further innovations in outlier detection. Two public health applications, CD4 cell counts in individuals and malnutrition data at national levels, displayed how information may be extracted from the sparse two-stage functional boxplot and the intensity sparse two-stage functional boxplot. Extensions of the methods proposed in this article to sparse images and surfaces could be explored with the surface boxplot (Genton et al. 2014).

Supplementary Materials

Supplements: *R-code for sparse and intensity functional boxplots:* R-code for the commands `sparse_fbplot` and `intensity_sparse_fbplot` described in the articles (`sparse_fbplot.R` & `intensity_sparse_fbplot.R`). *Simulation code:* Simulation code for the optimal depth under eight models described in the article (`00_execute_simulation_spearman.R`) and the outlier detection under eight models described in the article (`execute_outldetect.R`). *CD4 data:* CD4 count for 366 subjects from 18 months before to 42 months after seroconversion, load `cd4` (Goldsmith, Greven, and Crainiceanu 2013) in `refund` package. *Malnutrition data:* The original sparse prevalence of stunted growth and low birth height from 1985 to 2019 (`malnutrition.csv`). *Supplementary Material:* The performances of several depths and outlier detection under eight models in different sparseness types. All files can be found in a single zip file (`sparse_fbplot.zip`).

Funding

This research was supported by the King Abdullah University of Science and Technology (KAUST).

ORCID

Zhuo Qu  <http://orcid.org/0000-0001-5805-6101>
Marc G. Genton  <https://orcid.org/0000-0001-6467-2998>

References

- Arribas-Gil, A., and Romo, J. (2014), “Shape Outlier Detection and Visualization for Functional Data: The Outliergram,” *Biostatistics*, 15, 603–619. [976]
- Baddeley, A., Turner, R., Ruba, E., Berthelsen, K. K., Choiruddin, A., Coeurjolly, J.-F., Cronie, O., Davies, T., Fend, C., Gilbey, J., Guan, Y., Hahn, U., Hingee, K., Jalilian, A., Lavancier, F., van Lieshout, M.-C., McSwiggan, G., Rajala, T., Rakshit, S., Schuhmacher, D., Waagepetersen, R. P., Wang, H. (2022), “Package ‘spatstat.core’,” available at <https://cran.r-project.org/web/packages/spatstat.core/spatstat.core.pdf>. Accessed: 2022-02-16. [981]
- Claeskens, G., Hubert, M., Slaets, L., and Vakili, K. (2014), “Multivariate Functional Halfspace Depth,” *Journal of the American Statistical Association*, 109, 411–423. [976,988]
- Crainiceanu, C. M., and Goldsmith, A. J. (2010), “Bayesian Functional Data Analysis using WinBUGS,” *Journal of Statistical Software*, 32, 1–33. [986]
- Cuesta-Albertos, J. A., and Nieto-Reyes, A. (2008), “The Random Tukey Depth,” *Computational Statistics & Data Analysis*, 52, 4979–4988. [976]
- Cuevas, A., Febrero, M., and Fraiman, R. (2007), “Robust Estimation and Classification for Functional Data via Projection-Based Depth Notions,” *Computational Statistics*, 22, 481–496. [976]
- Dai, W., and Genton, M. G. (2018a), “Functional Boxplots for Multivariate Curves,” *Stat*, 7, e190. [976,980,982,988]
- (2018b), “Multivariate Functional Data Visualization and Outlier Detection,” *Journal of Computational and Graphical Statistics*, 27, 923–934. [976,982]
- Dai, W., and Genton, M. G. (2019), “Directional Outlyingness for Multivariate Functional Data,” *Computational Statistics & Data Analysis*, 131, 50–65. [976,982,988]

- Diggle, P. (1985), "A Kernel Method for Smoothing Point Process Data," *Journal of the Royal Statistical Society, Series C*, 34, 138–147. [980]
- Genton, M. G., Johnson, C., Potter, K., Stenchikov, G., and Sun, Y. (2014), "Surface Boxplots," *Stat*, 3, 1–11. [976,988]
- Genton, M. G., and Sun, Y. (2020), "Functional Data Visualization," in *Wiley StatsRef: Statistics Reference Online*, ed. M. Davidian, R. S. Kenett, N. T. Longford, G. Molenberghs, W. W. Piegorsch, and F. Ruggeri, pp. 1–11, Wiley Online Library: Wiley. [977]
- Gneiting, T., Kleiber, W., and Schlather, M. (2010), "Matérn Cross-Covariance Functions for Multivariate Random Fields," *Journal of the American Statistical Association*, 105, 1167–1177. [983]
- Goldsmith, J., Greven, S., and Crainiceanu, C. (2013), "Corrected Confidence Bands for Functional Data Using Principal Components," *Biometrics*, 69, 41–51. [977,979,986,988]
- Happ, C. (2018), "MFPCA: Multivariate Functional Principal Component Analysis for Data Observed on Different Dimensional Domains," *R package version*, 1. [978]
- Happ, C., and Greven, S. (2018), "Multivariate Functional Principal Component Analysis for Data Observed on Different (Dimensional) Domains," *Journal of the American Statistical Association*, 113, 649–659. [977,978,979,988]
- Hardin, J., and Rocke, D. M. (2005), "The Distribution of Robust Distances," *Journal of Computational and Graphical Statistics*, 14, 928–946. [982]
- HIV.gov (2020), "Symptoms of HIV," available at <https://www.hiv.gov/hiv-basics/overview/about-hiv-and-aids/symptoms-of-hiv>. Accessed: 2020-12-07. [986]
- Hsing, T., and Eubank, R. (2015), *Theoretical Foundations of Functional Data Analysis, with an Introduction to Linear Operators* (Vol. 997), Chichester: Wiley. [978]
- Hubert, M., Rousseeuw, P. J., and Segaert, P. (2015), "Multivariate Functional Outlier Detection," *Statistical Methods & Applications*, 24, 177–202. [979]
- Hyndman, R. J., and Shang, H. L. (2010), "Rainbow Plots, Bagplots, and Boxplots for Functional Data," *Journal of Computational and Graphical Statistics*, 19, 29–45. [976]
- Ibrahim, J. G., and Molenberghs, G. (2009), "Missing Data Methods in Longitudinal Studies: A Review," *TEST*, 18, 1–43. [976]
- Ieva, F., and Paganoni, A. M. (2013), "Depth Measures for Multivariate Functional Data," *Communications in Statistics-Theory and Methods*, 42, 1265–1276. [976]
- Ihaka, R., and Gentleman, R. (1996), "R: A Language for Data Analysis and Graphics," *Journal of Computational and Graphical Statistics*, 5, 299–314. [978]
- James, G. M., Hastie, T. J., and Sugar, C. A. (2000), "Principal Component Models for Sparse Functional Data," *Biometrika*, 87, 587–602. [977]
- Kendall, M. G. (1945), "The Treatment of Ties in Ranking Problems," *Biometrika*, 33, 239–251. [983]
- Li, C., Xiao, L., and Luo, S. (2020), "Fast Covariance Estimation for Multivariate Sparse Functional Data," *Stat*, 9, e245. [977]
- Liu, C., Ray, S., and Hooker, G. (2017), "Functional Principal Component Analysis of Spatially Correlated Data," *Statistics and Computing*, 27, 1639–1654. [977]
- López-Pintado, S., and Romo, J. (2009), "On the Concept of Depth for Functional Data," *Journal of the American Statistical Association*, 104, 718–734. [976,986,988]
- (2011), "A Half-Region Depth for Functional Data," *Computational Statistics & Data Analysis*, 55, 1679–1695. [976]
- López-Pintado, S., Sun, Y., Lin, J. K., and Genton, M. G. (2014), "Simplicial Band Depth for Multivariate Functional Data," *Advances in Data Analysis and Classification*, 8, 321–338. [976]
- López-Pintado, S., and Wei, Y. (2011), "Depth for Sparse Functional Data," in *Recent Advances in Functional Data Analysis and Related Topics*, ed. F. Ferraty, pp. 209–212, Berlin: Springer. [976,977,979]
- Mirzargar, M., Whitaker, R. T., and Kirby, R. M. (2014), "Curve Boxplot: Generalization of Boxplot for Ensembles of Curves," *IEEE Transactions on Visualization and Computer Graphics*, 20, 2654–2663. [976]
- Narisetty, N. N., and Nair, V. N. (2016), "Extremal Depth for Functional Data and Applications," *Journal of the American Statistical Association*, 111, 1705–1714. [976]
- Qu, Z., Dai, W., and Genton, M. G. (2021), "Robust Functional Multivariate Analysis of Variance with Environmental Applications," *Environmetrics*, 32, e2641. [976]
- Ramsay, J. O., and Dalzell, C. (1991), "Some Tools for Functional Data Analysis," *Journal of the Royal Statistical Society, Series B*, 53, 539–561. [976]
- Renardy, M., and Rogers, R. C. (2006), *An Introduction to Partial Differential Equations* (Vol. 13), New York: Springer. [978]
- Rousseeuw, P. J. (1984), "Least Median of Squares Regression," *Journal of the American Statistical Association*, 79, 871–880. [982]
- Rousseeuw, P. J., and Van Driesssen, K. (1999), "A Fast Algorithm for the Minimum Covariance Determinant Estimator," *Technometrics*, 41, 212–223. [982]
- Sguera, C., Galeano, P., and Lillo, R. (2014), "Spatial Depth-Based Classification for Functional Data," *TEST*, 23, 725–750. [976]
- Sguera, C., and López-Pintado, S. (2021), "A Notion of Depth for Sparse Functional Data," *TEST*, 30, 630–649. [977,979]
- Sun, Y., and Genton, M. G. (2011), "Functional Boxplots," *Journal of Computational and Graphical Statistics*, 20, 316–334. [976,980,982,988]
- (2012a), "Adjusted Functional Boxplots for Spatio-Temporal Data Visualization and Outlier Detection," *Environmetrics*, 23, 54–64. [976]
- (2012b), "Functional Median Polish," *Journal of Agricultural, Biological, and Environmental Statistics*, 17, 354–376. [976]
- Taylor, J., Fahey, J. L., Detels, R., and Giorgi, J. V. (1989), "CD4 Percentage, CD4 Number, and CD4: CD8 Ratio in HIV Infection: Which to Choose and How to Use," *Journal of Acquired Immune Deficiency Syndromes*, 2, 114–124. [986]
- Thompson, W. K., and Rosen, O. (2008), "A Bayesian Model for Sparse Functional Data," *Biometrics*, 64, 54–63. [977]
- Tukey, J. W. (1975), "Mathematics and the Picturing of Data," in *Proceedings of the International Congress of Mathematicians, Vancouver, 1975* (Vol. 2). pp. 523–531. [976,979]
- (1977), *Exploratory Data Analysis* (Vol. 2), Reading, MA: Addison-Wesley Pub. Co. [980]
- UNICEF (2020), "Malnutrition," available at [United Nations Development Programme \(2019\), "Human Development Report 2019," available at <https://hdr.undp.org/sites/default/files/hdr2019.pdf>. Accessed: 2022-01-30. \[987\]

Xiao, L., Li, C., Checkley, W., and Crainiceanu, C. \(2018\), "Fast Covariance Estimation for Sparse Functional Data," *Statistics and Computing*, 28, 511–522. \[977\]

Yao, F., Müller, H.-G., and Wang, J.-L. \(2005\), "Functional Linear Regression Analysis for Longitudinal Data," *The Annals of Statistics*, 33, 2873–2903. \[977,988\]

Yao, Z., Dai, W., and Genton, M. G. \(2020\), "Trajectory Functional Boxplots," *Stat*, 9, e289. \[976\]

Zhou, L., Huang, J. Z., and Carroll, R. J. \(2008\), "Joint Modelling of Paired Sparse Functional Data Using Principal Components," *Biometrika*, 95, 601–619. \[977\]

Zuo, Y., and Serfling, R. \(2000\), "General Notions of Statistical Depth Function," *The Annals of Statistics*, 28, 461–482. \[979\]](https://data.unicef.org/resources/data_explorer/unicef_f?g=UNICEF&df=GLOBAL_DATAFLOW&ver=1.0&dq=NT_ANT_WHZ_NE3+NT_ANT_HAZ_NE2+NT_B_W_LBW+NT_ANT_WHZ_NE2..&startPeriod=2016&endPeriod=)